

An Efficient Rescaling Algorithm for Simulating the Evolution of Multiple Elastically Stressed Precipitates

Amlan K. Barua¹, Shuwang Li^{1,*}, Hualong Feng¹, Xiaofan Li¹ and John Lowengrub²

¹ Department of Applied Mathematics, Illinois Institute of Technology, Chicago 60616, USA.

² Department of Mathematics, University of California at Irvine, Irvine, CA 92697, USA.

Received 25 October 2012; Accepted (in revised version) 27 December 2012

Communicated by Bo Li

Available online 19 March 2013

Abstract. In this paper, we propose a space-time rescaling scheme for computing the long time evolution of multiple precipitates in an elastically stressed medium. The algorithm is second order accurate in time, spectrally accurate in space and enables one to simulate the evolution of precipitates in a fraction of the time normally used by fixed-frame algorithms. In particular, we extend the algorithm recently developed for single particle by Li et al. (Li, Lowengrub and Leo, *J. Comput. Phys.*, 335 (2007), 554) to the multiple particle case, which involves key differences in the method. Our results show that without elasticity there are successive tip splitting phenomena accompanied by the formation of narrow channels between the precipitates. In presence of applied elastic field, the precipitates form dendrite-like structures with the primary arms aligned in the principal directions of the elastic field. We demonstrate that when the far-field flux decreases with the effective radius of the system, tip-splitting and dendrite formation can be suppressed, as in the one particle case. Depending on the initial position of the precipitates, we further observe that some precipitates grow while others may shrink, even when a positive far field flux is applied.

AMS subject classifications: 74N25, 74B15

Key words: Diffusion, elasticity, dendrite, side branching, boundary integral method.

1 Introduction

The growth of precipitates in an elastic matrix is an important problem in the metal industry. One example is the production of alloys (e.g. [Al-Ni]) by solid/solid phase

*Corresponding author. *Email addresses:* abarua@iit.edu (A. K. Barua), sli@math.iit.edu (S. Li), hfeng@iit.edu (H. Feng), lix@iit.edu (X. Li), lowengrub@math.uci.edu (J. Lowengrub)

transformations, in which the metal mixture is suddenly driven out of its initial equilibrium state by lowering the temperature. As a consequence, precipitates nucleate within the bulk material and forms a new dispersed (precipitate) phase with different material properties. The precipitates undergo diffusional growth until a new thermodynamic equilibrium state between the precipitates and matrix is reached.

Since the features of the microscopic precipitates determine the macroscopic properties of the material (e.g., stiffness, strength and toughness), there have been many computational investigations of phase transformations in metallic alloys (e.g., [1,2,6,15,17,18,21,27,30,33,38,39,41–43,46,48]). Under appropriate assumptions, the diffusional growth system can be posed as a moving boundary problem. From an analytical perspective, Mullins and Sekerka proposed a linear stability theory to address the evolution of a single, slightly perturbed spherical precipitate [32], which was later generalized to consider elastic stresses [15,20,22]. As perturbations grow, nonlinearity becomes important and the precipitate develops complex dendritic, or ramified, morphologies. Computer simulations have then been used to study this nonlinear phenomenon.

Boundary integral methods are one of the most accurate numerical techniques for simulating free boundary problems. Such methods can be made very efficient through the use of fast solvers, such as the fast multipole method (e.g., [8,13,19,49]) or tree algorithms (e.g., [10,28,35,47]) among others and the fact that the dimension of the problem is reduced by one. Other methods for simulating microstructure dynamics include level-set and phase-field methods, which have their own advantages and disadvantages. See for example the reviews [5,16,18,23,34,37,43].

Following S. Mikhlin's approach [31], Greenbaum et al. developed an efficient boundary integral method for solving the quasi-steady diffusion problem in a multiply connected domain and evaluated the Dirichlet Neumann mapping [11]. This approach was later used in [4,14] and [15,21] to perform simulations of precipitate dynamics with and without elastic stresses in two dimensions, respectively. Other boundary integral methods have also been used to study two dimensional precipitate evolution, see e.g., [1,38–42,44,45] among others. Three dimensional boundary integral simulations of precipitate dynamics can be found in [9,27].

There are numerous difficulties associated with simulating the long-time evolution of single and multiple precipitates. First, the morphologies tend to be complex. Second, the precipitates grow in size, which together with the complex morphologies, increases the range of scales that need to be resolved. Third, although the precipitates are growing, their rate of growth slows as time increases. This makes long-time simulations of precipitate growth expensive. We address these issues by extending a space-time rescaling scheme, originally developed for single particles [3,26] to the multiple particle case. The extension involves key differences in the algorithm. The idea is to rescale time and space such that the precipitate evolves exponentially fast in the rescaled frame and does not change size in the rescaled frame. We demonstrate that the algorithm, which is second order accurate in time and spectrally accurate in space, is able to simulate the evolution of precipitates in a fraction of the time normally used by fixed-frame algorithms.

We present long-time simulations of microstructures containing multiple particles under different growth conditions with and without elastic stresses.

This paper is organized as follows. In Section 2, we present the mathematical formulation. In Section 3, we describe the boundary integral formulation. In Section 4, we describe the rescaling scheme for multiple precipitates. In Section 5, we discuss the numerical results. In Section 6, we give concluding remarks and discuss future work.

2 Mathematical formulation

2.1 The diffusion problem

We assume the matrix and precipitates occupy regions in a two-dimensional plane. The precipitate phase Ω^P consists of p precipitates occupying separate bounded regions Ω_i^P . The matrix phase Ω^M is an unbounded region exterior to the precipitates. The boundary between the i th precipitate and the matrix phase is Γ_i . The total interface $\Gamma = \cup_{i=1}^p \Gamma_i$ separates the matrix and precipitate phase. A circular far-field boundary Γ_∞ at R_∞ encloses all precipitates and appears in the problem in a limiting sense $R_\infty \rightarrow \infty$, see Fig. 1 and Eq. (2.1c) below.

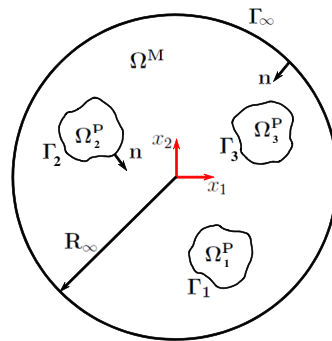


Figure 1: Schematic diagram of a two phase domain. Three precipitates occupy regions Ω_1^P , Ω_2^P and Ω_3^P . They are surrounded by matrix of infinite extent Ω^M . The interface separating the two phases is $\Gamma = \cup_i \Gamma_i$. A limiting far-field boundary Γ_∞ encloses all the precipitates.

Following [15], we assume that diffusion only occurs in the matrix phase and we nondimensionalize the system using the initial precipitate radius to be the length scale and the diffusion time to be the time scale. Let U be the concentration of the diffusing species in the matrix phase, then under a quasi-static assumption U satisfies the Laplace equation,

$$\nabla^2 U = 0 \quad \text{in } \Omega^M \subset \mathcal{R}^2, \tag{2.1a}$$

$$U = \kappa \quad \text{on } \Gamma = \cup_{i=1}^n \Gamma_i, \tag{2.1b}$$

$$\lim_{R_\infty \rightarrow \infty} \frac{1}{2\pi} \int_{\Gamma_\infty} \nabla U \cdot \mathbf{n} \, ds = -J, \tag{2.1c}$$

together with the mass balance equation across Γ_i :

$$V^i = \frac{\partial U}{\partial \mathbf{n}} \quad \text{on } \Gamma_i. \quad (2.2)$$

In the above equations, κ is the curvature of the interface, \mathbf{n} is the normal, J is the total applied mass flux and V^i is the normal velocity of the interface between the i th precipitate and matrix. A positive J indicates mass enters the system. Since U is harmonic, we have an alternative expression of Eq. (2.1c),

$$0 = \int_{\Omega^M} \nabla^2 U d\Omega = \int_{\Gamma} \nabla U \cdot \mathbf{n} ds + \lim_{R \rightarrow \infty} \int_{\Gamma = \partial B[0;R]} \nabla U \cdot \mathbf{n} ds = \int_{\cup_{i=1}^p \Gamma_i} V^i ds - 2\pi J. \quad (2.3)$$

If the evolution takes place in presence of the elasticity, then the boundary condition Eq. (2.1b) becomes

$$U = \kappa + Z G_{el}, \quad (2.4)$$

where G_{el} is the elastic energy density and the parameter Z characterizes the relative contribution of stress. The computation of G_{el} requires one to solve the elasticity problem in both phases [15, 20].

2.2 The elasticity problem

Following [15, 22], G_{el} is calculated by

$$G_{el} = \frac{1}{2} \sigma_{ij}^P (\epsilon_{ij}^P - \epsilon_{ij}^T) - \frac{1}{2} \sigma_{ij}^M \epsilon_{ij}^M + \sigma_{ij}^M (\epsilon_{ij}^M - \epsilon_{ij}^P), \quad (2.5)$$

where ϵ_{ij} and σ_{ij} are the strain and stress tensors in the matrix phase (superscript M) and precipitate phase (superscript P), respectively. The superscript T denotes the transformation (misfit) strain of the precipitate due to the mismatch of the crystal lattice between the precipitate and the matrix phase. For simplicity, we assume both precipitate and the matrix phase are elastically linear and isotropic (the formulation can be extended to incorporate anisotropic elasticity [21]). The Poisson ratio and shear modulus of the phases are denoted respectively by μ^χ and ν^χ , where χ can be either "M" or "P".

In the absence of body forces, the elasticity problem is posed as,

$$\sigma_{ij,j}^\chi = 0 \quad \text{in } \Omega^\chi, \quad (2.6a)$$

$$u_i^P = u_i^M \quad \text{on } \Gamma, \quad (2.6b)$$

$$\sigma_{ij}^P n_j = \sigma_{ij}^M n_j \quad \text{on } \Gamma, \quad (2.6c)$$

$$\lim_{r \rightarrow \infty} \epsilon_{ij}^M = \epsilon_{ij}^0. \quad (2.6d)$$

Eq. (2.6a) describes force balance equations. Eqs. (2.6b) and (2.6c) describe the continuity of displacement and traction across the interface Γ , respectively (coherent boundary conditions). Eq. (2.6d) is the applied far-field boundary condition. We have used the Einstein

summation convention in the above equations (and in the remainder of the paper) with indices i and j running from 1 to 2. Considering the misfit strain, the constitutive laws for the precipitates and the matrix are given by

$$\sigma_{ij}^P = C_{ijkl}^P (\epsilon_{kl}^P - \epsilon_{kl}^T), \quad \sigma_{ij}^M = C_{ijkl}^M \epsilon_{kl}^M, \quad (2.7)$$

where the isotropic stiffness tensor

$$C_{ijkl}^\chi = 2\mu^\chi \left[\frac{\nu^\chi}{1-2\nu^\chi} \delta_{kl} \delta_{ij} + \delta_{ik} \delta_{jl} \right] \quad (2.8)$$

and δ_{ij} is the Kronecker delta. Once the equations of elasticity are solved, one can compute the elastic energy density G_{el} using Eq. (2.5).

3 Boundary integral formulation

3.1 The diffusion problem

Using the complex variable $z = x_1 + ix_2$ to denote computational points on the interface, we write boundary integral equations for the diffusion problem in terms of an unknown dipole density function ϕ defined on Γ and unknown p source terms B_1, B_2, \dots, B_p , corresponding to the p precipitates [11, 15, 31]:

$$\left(-\frac{1}{2}\mathcal{I} + K \right) [\phi] + \sum_{k=1}^p B_k \log |z(s,t) - S_k| = \kappa + ZG^{el}, \quad (3.1a)$$

$$\sum_{k=1}^p B_k = J, \quad (3.1b)$$

$$\int_{r_j} \phi(s',t) ds' = 0, \quad j = 1, \dots, p-1, \quad (3.1c)$$

where $S_k = x_{1k} + ix_{2k}$ is a point inside the closed interface Γ_k and the integral operator

$$K[\phi](s,t) = \frac{1}{2\pi} \int_{\Gamma} \phi(s',t) \left[\frac{\partial}{\partial n(s',t)} \log |z(s',t) - z(s,t)| + 1 \right] ds'. \quad (3.2)$$

3.2 The elasticity problem

The fundamental solutions in terms of the displacement and traction are given by the Kelvin function,

$$U_{jk}(z, z') = \frac{1}{8\pi\mu(1-\nu)} \left[(3-4\nu) \ln \left(\frac{1}{r} \right) \delta_{jk} + r_{,j'} r_{,k'} \right], \quad (3.3a)$$

$$T_{jk}(z, z') = \frac{-1}{4\pi(1-\nu)r} \left[\frac{\partial r}{\partial n'} ((1-2\nu)\delta_{jk} + 2r_{,j'} r_{,k'}) + (1-2\nu)(n'_{,j} r_{,k'} - n'_{,k} r_{,j'}) \right], \quad (3.3b)$$

where $r = |z' - z|$, $r_{,k'} = \partial r / \partial x'_k$ and n'_k is the k th component of the normal at point z' . An outline of the derivation for these fundamental solutions can be found in [7, 15].

Using the fundamental solutions as a test function, we multiply $\sigma_{kj,j}^P = 0$ by U_{jk} and integrate over Ω_i^P . Then we perform integration by parts twice and apply the divergence theorem. Taking the interfacial limit, we write the solution to the elasticity problem as a set of coupled boundary integral equations for the precipitate and matrix phases. For the precipitate phases, we have

$$\frac{1}{2}u_j^P + \int_{\Gamma_i} u_k^P T_{jk}^P ds' - \int_{\Gamma_i} t_k^P U_{jk}^P ds' = \int_{\Gamma_i} t_k^T U_{jk}^P ds', \quad j=1,2, \quad (3.4)$$

where u_j^P denotes the unknown displacement vector and t_j^P denotes the unknown traction vector of a point on the interface Γ_i . The quantity $t_j^T = \sigma_{jk}^T n_k$ is a given traction due to the misfit strain [15]. The boundary integral equation for the matrix phase, with u_j^M and t_j^M as unknowns, is

$$\frac{1}{2}u_j^M - \int_{\Gamma} u_k^M T_{jk}^M ds' + \int_{\Gamma} t_k^M U_{jk}^M ds' = \frac{1}{2}u_j^0 - \int_{\Gamma} u_k^0 T_{jk}^M ds' + \int_{\Gamma} t_k^0 U_{jk}^M ds', \quad (3.5)$$

where $u_k^0 = \epsilon_{kj}^0 x_j$ is the k th component of the displacement due to the applied strain and t_k^0 is the corresponding traction. Note that in Eq. (3.5), the integration is over the entire interface Γ separating the precipitate and matrix phases.

Since the traction and the displacement are continuous across the interface, $u_j^P = u_j^M$ and $t_j^P = t_j^M$, we drop the superscripts and simply write these quantities as u_j and t_j . Then Eqs. (3.4) and (3.5) become

$$\frac{1}{2}u_j + \int_{\Gamma_i} u_k T_{jk}^P ds' - \int_{\Gamma_i} t_k U_{jk}^P ds' = \int_{\Gamma_i} t_k^T U_{jk} ds', \quad (3.6a)$$

$$\frac{1}{2}u_j - \int_{\Gamma} u_k T_{jk} ds' - \int_{\Gamma} t_k U_{jk}^M ds' = \frac{1}{2}u_j^0 - \int_{\Gamma} u_k^0 T_{jk}^M ds' - \int_{\Gamma} t_k^0 U_{jk}^M ds'. \quad (3.6b)$$

We solve these integrals equations for u_1, u_2 and t_1, t_2 and then compute G_{el} using Eq. (2.5). Note that this is a direct formulation of the elasticity equations. Other, indirect formulations have also been developed, e.g., [12, 29].

4 The rescaling scheme

The rescaling scheme developed in [26] is limited to a single interface (one precipitate) in an infinite matrix phase. The idea of the rescaling scheme in [26] is to scale out the overall growth by a scaling factor, which is derived using an imposed condition: the area of the precipitate in the rescaled frame is always conserved. In addition, time is rescaled

such that the area of the precipitate grows exponentially fast in the rescaled time. Here, we extend this approach to the case of multiple precipitates.

For multiple particles, the situation gets complicated because of the interaction between the precipitate and the matrix phases and interactions among the precipitates themselves. In particular, new length scales are introduced into the system – the distances between the precipitates – which typically decrease in the rescaled frame as time progresses. Further, to track the evolution of each individual precipitate, one has to compute the centroid of each individual precipitate. This ensures that the precipitate is placed at the right location and that the interactions with other precipitates can be computed properly. With this in mind, we introduce the following spatial and temporal scaling

$$\mathbf{x}^i(t) + \mathbf{x}_c^i(t) = \bar{R}(\bar{t}) (\bar{\mathbf{x}}^i(\bar{t}) + \bar{\mathbf{x}}_c^i(\bar{t})), \tag{4.1a}$$

$$\bar{t} = \int_0^t \frac{1}{f(t')} dt', \tag{4.1b}$$

where $R(t) = \bar{R}(\bar{t}(t))$ is a scaling factor, the superscript i denotes the i th precipitate centered at $\mathbf{x}_c^i(t)$, f is a function of time t that represents the temporal rescaling and the barred variables are quantities in the rescaled frame. We identify the interface of the i th precipitate using $\mathbf{x}^i(t, \alpha) + \mathbf{x}_c^i$, with α a parametrization of Γ_i and write its normal velocity as

$$V^i = \frac{d(\mathbf{x}^i + \mathbf{x}_c^i)}{dt} \cdot \mathbf{n} = \left(\bar{R} \frac{d(\bar{\mathbf{x}}^i + \bar{\mathbf{x}}_c^i)}{d\bar{t}} + (\bar{\mathbf{x}}^i + \bar{\mathbf{x}}_c^i) \frac{d\bar{R}}{d\bar{t}} \right) \frac{d\bar{t}}{dt} \cdot \bar{\mathbf{n}}. \tag{4.2}$$

Recalling Eq. (2.3), we obtain

$$\begin{aligned} J &= \frac{1}{2\pi} \int_{\cup_{i=1}^p \Gamma_i} V^i ds \\ &= \frac{1}{2\pi} \int_{\cup_{i=1}^p \bar{\Gamma}_i} \bar{R}^2 \frac{d\bar{t}}{dt} \frac{d(\bar{\mathbf{x}}^i + \bar{\mathbf{x}}_c^i)}{d\bar{t}} \cdot \bar{\mathbf{n}} d\bar{s} + \frac{1}{2\pi} \int_{\cup_{i=1}^p \bar{\Gamma}_i} \bar{R} \frac{d\bar{R}}{d\bar{t}} \frac{d\bar{t}}{dt} (\bar{\mathbf{x}}^i + \bar{\mathbf{x}}_c^i) \cdot \bar{\mathbf{n}} d\bar{s} \\ &= \frac{1}{2\pi} \int_{\cup_{i=1}^p \bar{\Gamma}_i} \bar{R}^2 \frac{d\bar{t}}{dt} \bar{V}^i d\bar{s} + \frac{1}{\pi} \bar{R} \frac{d\bar{R}}{d\bar{t}} \frac{d\bar{t}}{dt} \bar{A}, \end{aligned} \tag{4.3}$$

where

$$\bar{V}^i = \frac{d(\bar{\mathbf{x}}^i + \bar{\mathbf{x}}_c^i)}{d\bar{t}} \cdot \bar{\mathbf{n}}, \quad \bar{A} = \frac{1}{2} \int_{\cup_{i=1}^p \bar{\Gamma}_i} (\bar{\mathbf{x}}^i + \bar{\mathbf{x}}_c^i) \cdot \bar{\mathbf{n}} d\bar{s}. \tag{4.4}$$

Note that the quantity \bar{A} now represents the total area enclosed by all interfaces, i.e., $\bar{A} = \sum_{i=1}^p \bar{A}^i$. Imposing a total area conservation constraint $\int_{\cup_{i=1}^p \bar{\Gamma}_i} \bar{V}^i d\bar{s} = 0$ in the rescaled frame, we obtain

$$J = \frac{1}{\pi} \bar{A} \frac{\bar{R}}{f(\bar{t})} \frac{d\bar{R}}{d\bar{t}}. \tag{4.5}$$

Thus, with this choice of R , the total precipitate area does not change in the rescaled frame. To achieve an exponential growth rate $\bar{R}(\bar{t}) = \exp(\pi \bar{J} \bar{t} / \bar{A})$, we choose $f = R^2 \bar{J} / J$. For example, if the flux $J = \bar{J}$ is a constant, then $f = R^2$, or if $J = \bar{J} / R$ then $f = R^3$.

Finally, the centroid coordinates $\bar{\mathbf{x}}_c^i(\bar{t}) = (\bar{x}_c^i(\bar{t}), \bar{y}_c^i(\bar{t}))$ are updated using the following two equations

$$\frac{d\bar{x}_c^i}{d\bar{t}} = \frac{1}{\bar{A}^i(\bar{t})} \left[\int_{\Gamma_i} \bar{x}^i \bar{V}^i d\bar{s}_\alpha^i - \bar{x}_c^i(\bar{t}) \int_{\Gamma_i} \bar{V}^i d\bar{s}_\alpha^i \right], \tag{4.6a}$$

$$\frac{d\bar{y}_c^i}{d\bar{t}} = \frac{1}{\bar{A}^i(\bar{t})} \left[\int_{\Gamma_i} \bar{y}^i \bar{V}^i d\bar{s}_\alpha^i - \bar{y}_c^i(\bar{t}) \int_{\Gamma_i} \bar{V}^i d\bar{s}_\alpha^i \right], \tag{4.6b}$$

$i = 1, \dots, p$. In practice, we update the centroid using the second order Adams-Bashforth method.

However, updating $\bar{\mathbf{x}}^i$ by an explicit method suffers from severe stability constraints—the time step $\Delta t \sim \mathcal{O}(\Delta s^3)$, where Δs is the arclength spacing between interface marker points [14]. Thus, not only is there a high-order constraint, the clustering of marker points along the interface significantly exacerbates the stiffness. To overcome these problems, we follow the non-stiff time stepping method proposed by Hou et al. [14] and pose the dynamic equations using $L-\theta$ system, where L denotes the interface length and θ is the angle that the interface tangent makes with the x -axis (tangent angle). At time $t = 0$, the interface is discretized using marker points that are equally spaced along the interface. For the each precipitate interface Γ_i , we choose a special tangential velocity T^i to keep the marker points equally spaced at later times [14]. The equations of motion for the precipitate-matrix interfaces Γ_i then become

$$\bar{L}_t^i = \int_0^{2\pi} \bar{\theta}_\alpha^i \bar{V}^i(\alpha, t) d\alpha, \tag{4.7a}$$

$$\bar{\theta}_t^i = \frac{2\pi}{\bar{L}^i} (-\bar{V}_\alpha^i + \bar{T}^i \bar{\theta}_\alpha^i). \tag{4.7b}$$

Following the small scale decomposition technique [14] where the highest order term is identified and integrated explicitly using an integrating factor, Eq. (4.7b) is solved by a semi implicit integrating factor method. Eq. (4.7a) is updated using the second order Adams-Bashforth method.

4.1 Rescaling of elasticity integral equations

Define \bar{u} and \bar{t}_j with $u = \bar{R}\bar{u}$ and $t_j = \bar{t}_j$. A straightforward calculation shows that the form of the elasticity integral equations remains unchanged with these new barred variables. Further, there is no need to rescale the elastic energy as it remains unchanged in the rescaled frame, i.e., $G_{el} = \bar{G}_{el}$.

4.2 Rescaling of diffusion integral equations

The curvature of the rescaled interface is related to the original by $\bar{\kappa} = \bar{R}\kappa$. Introducing rescaled dipole density $\bar{\phi} = \bar{R}\phi$ and rescaled source terms $\bar{B}_k = \bar{R}B_k$, Eqs. (3.1a), (3.1b) and (3.1c) become

$$-\frac{1}{2}\bar{\phi}(\bar{s},\bar{t}) + \frac{1}{2\pi} \int_{\bar{\Gamma}} \bar{\phi}(\bar{s}',\bar{t}) \left[\frac{\partial}{\partial \bar{n}(\bar{s}',\bar{t})} \log |\bar{z}(\bar{s}',\bar{t}) - \bar{z}(\bar{s},\bar{t})| + \bar{R} \right] d\bar{s}' + \sum_{k=1}^p \bar{B}_k \log \bar{R} |z(\bar{s},\bar{t}) - S_k| = \bar{Z}\bar{G}_{el} + \bar{\kappa}, \tag{4.8a}$$

$$\sum_{k=1}^p \bar{B}_k = \bar{J}, \tag{4.8b}$$

$$\int_{\Gamma_j} \bar{\phi}(\bar{s}',\bar{t}) d\bar{s}' = 0, \quad j = 1, \dots, p-1, \tag{4.8c}$$

where $\bar{Z} = \bar{R}Z$.

4.3 Rescaling of Dirichlet Neumann map

The Dirichlet Neumann map, which is used to compute the velocity, takes the following form in the rescaled frame

$$\begin{aligned} \bar{V} &= \frac{d\bar{\mathbf{x}}}{d\bar{t}} \cdot \bar{\mathbf{n}} \\ &= \frac{f}{\bar{R}} \left(\frac{1}{2\pi\bar{R}^2} \int_{\bar{\Gamma}} \bar{\phi}_{,s'} \frac{\partial}{\partial \bar{s}} \log |\bar{z}(s') - \bar{z}(s)| d\bar{s}' \right. \\ &\quad \left. + \sum_{k=1}^p \frac{\bar{B}_k}{\bar{R}^2} \frac{(\bar{x}_1 - \bar{x}_{1k})\bar{x}_{2,s} - (\bar{x}_2 - \bar{x}_{2k})\bar{x}_{1,s}}{(\bar{x}_1 - \bar{x}_{1k})^2 + (\bar{x}_2 - \bar{x}_{2k})^2} - \frac{\pi J}{A\bar{R}} \bar{\mathbf{x}} \cdot \bar{\mathbf{n}} \right), \end{aligned} \tag{4.9}$$

where $\bar{x}_{j,\bar{s}} = \frac{\partial \bar{x}_j}{\partial \bar{s}}$.

4.4 Algorithm

In practice, we first solve the elasticity equation to compute G_{el} term for the diffusion problem. We then solve the diffusion problem, compute the normal velocity and update the interface. The preconditioners for the diffusion and elasticity problems are derived using the small scale decomposition(SSD) of the kernels [15]. The idea of SSD is to extract the dominant part of the equations at small spatial scales [14]. SSD has been successfully implemented in the context of Hele-Shaw problem [14, 25, 26], evolution of an epitaxial thin film [24], crystal growth [3] and dynamics of inextensible vesicles [36]. The overall algorithm is given below.

Algorithm 4.1: Numerical algorithm

 Input: starting shapes \bar{x}

1. at $t=0$ perform equal arclength discretization
 2. **for** $t=0$ to t_{final} **do**
 3. discretize elasticity equations using alternating point quadrature
 4. solve discrete system using preconditioned GMRES
 5. compute G_{el}
 6. discretize diffusion equation using alternating point quadrature
 7. solve discrete system using preconditioned GMRES
 8. compute normal velocity \bar{V}
 9. construct tangential velocity \bar{T}
 10. update interface \bar{x}
 11. **end for**
-

5 Results and discussions

All simulations are carried out on a cluster having 16 nodes. Each node has two Intel(R) Xeon(R) 2.53GHz processors, each of which has 4 cores (total 8 cores per node). Each node also has 24GB memory, with 3GB for each core, so the memory is not shared between processor cores. There is infiniband connection between nodes. The diffusion problem with N marker points on each interface corresponds to a matrix of size $(pN+p-1) \times (pN+p-1)$. To solve the elasticity problem one needs to compute two components of the displacement and another two components of the traction for each marker point on the interface. Thus the matrix size is $(4pN \times 4pN)$. To reduce the cost of matrix vector multiplications from $\mathcal{O}(N^2)$ to $\mathcal{O}(N \log N)$, we implement an adaptive tree code method to compute the matrix-vector product in the GMRES solvers for both diffusion and elasticity problems [10]. If necessary (especially when the precipitate morphologies become complicated and N is large), we use a source dividing strategy to parallelize the code in which the source points are evenly divided among all the processors [10].

For the diffusion problem, at early times the iteration number of GMRES is about 4 and then slowly increases to about 20 at later times as the morphologies of the precipitates get complicated. For the elasticity problem, at early times the iteration number of GMRES is about 7 and the number of iteration is roughly four times the iteration number for the diffusion problem at later times. Note that for the elasticity problem we solve four integral equations (two for the displacement and two for the stress).

5.1 Performance of the algorithm

5.1.1 Convergence test

We use two circular precipitates of unit radius centered at (3,0) and (0,3). The far-field flux is $J=25$.

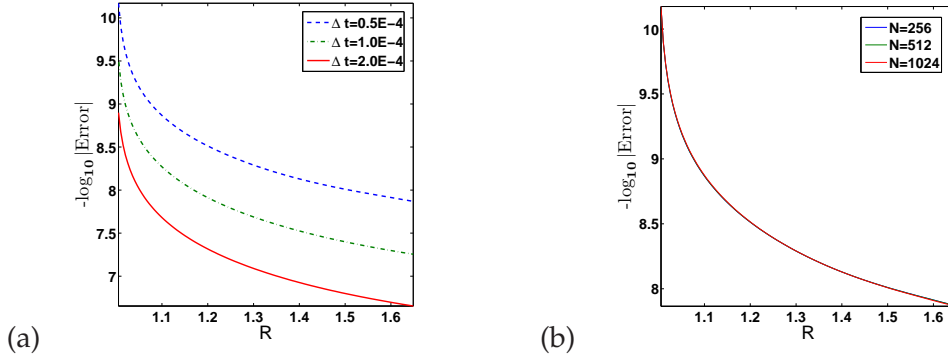


Figure 2: (a) Numerical evidence of second order convergence in time of the total area of the precipitates. (b) Numerical evidence of the spectral accuracy of the scheme for the total area of the precipitates.

To check the temporal convergence, we take $N = 512$ marker points on each interface and run the code to $\bar{t} = 0.04$ using time steps $\Delta \bar{t} = 2 \times 10^{-4}$, 1×10^{-4} and 5×10^{-5} . We use the total area of the two particles \bar{A} to measure the numerical error

$$err = |\bar{A}(0, N = 512) - \bar{A}(\Delta \bar{t}, N = 512)| \quad (5.1)$$

for the three different time steps $\Delta \bar{t}$. Fig. 2(a) shows a plot of $-\log_{10}(err)$ versus the scaling factor $R(\bar{t})$. We see that the curves are separated by an amount of 0.6 when the time step is halved. Thus the second order convergence in time is confirmed.

To check the spectral accuracy, we use a fixed time step $\Delta \bar{t} = 5 \times 10^{-5}$ and run simulations with $N = 256, 512, 1024$ points up to $\bar{t} = 0.04$. Note that we can use much large time steps, but for the purpose of accuracy we choose a small one. The numerical error $err = |\bar{A}(t = 0, N) - \bar{A}(\bar{t}, N)|$ is plotted against $R(\bar{t})$ in Fig. 2(b). The curves superimpose on each other suggesting spectral accuracy. In practice, we notice when the precipitates get close to each other (around the grid resolution, h), the spectral accuracy is lost if no refinement of the interfaces is made.

5.1.2 Comparison with results from the original unscaled algorithm

We demonstrate the equivalence between the rescaled and original formulation by comparing a shape factor

$$(\delta/R)_i = \max_{\alpha} \left| |\bar{\mathbf{x}}|^i / R_{eq}^i - 1 \right|, \quad (5.2)$$

where R_{eq}^i is the equivalent radius of the i th shape, $R_{eq}^i = \sqrt{A_i/\pi}$. Note that A_i is used rather than \bar{A}_i so that the equivalent radius is defined in the original frame. In absence of elasticity, we use the same test case as Fig. 2. We plot the shape factors of the precipitate initially located at $(0,3)$ obtained from the scaled and the original code against time in Fig. 3(a). The shape factors match exactly, which confirms that the rescaled and the original formulation produce identical results.

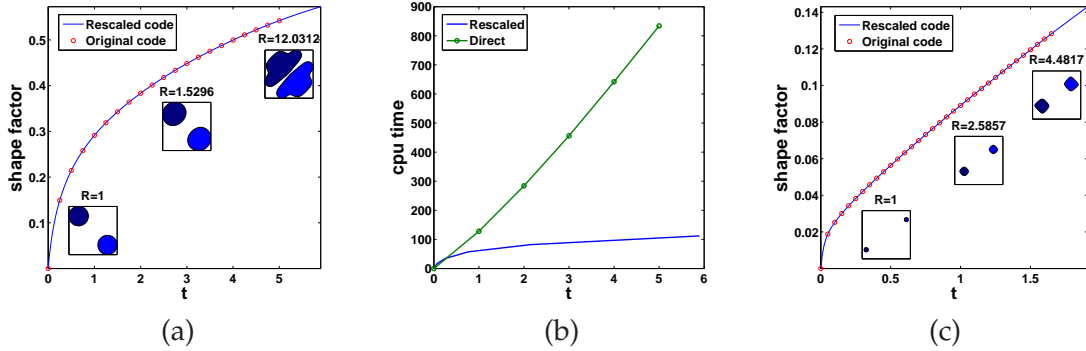


Figure 3: (a) Evolution of the shape factor of two circular particles that are initially centered at $(3,0)$ and $(0,3)$ and have unit radius. The flux is $J=25$. We show the shape factors of the precipitate initially located at $(0,3)$ using the original (circles) and rescaled (line) algorithms. Insets show the configuration of the particles at different times of evolution, labeled according to the scale factor R . (b) A comparison of the CPU times shows that the rescaled scheme (line) is much more efficient than the original (line with circular marker points). (c) Evolution of the shape factors of two particles growing in presence of elastic fields with $J=10$. The elastic field is generated due to an applied shear with $\epsilon_{11}^0 = \epsilon_{22}^0 = -0.02$ and $Z=6000$. The particles are initially located at $(-10, -7.5)$ and $(10, -7.5)$ and have unit radii.

The speed gain due to exponential scaling is significant. For example, using a time step $\Delta \bar{t} = 1 \times 10^{-4}$ we run the rescaled code up to time $\bar{t} = 0.20$, which corresponds roughly to the time $t = 5.85$ in the unscaled frame. It takes roughly 112 seconds CPU time to finish the computation. We run the original code up to time $t = 5$ using a much larger time step 5×10^{-3} . It takes roughly 850 seconds CPU time to complete the calculation. Even at this early stage, the computation is roughly eight times faster as shown in Fig. 3(b). From the steep rise of the CPU time curve for the original formulation, the gain will be dramatically higher at later times for the rescaled scheme.

In presence of elasticity, we consider parameters $Z = 6000$ and $J = 10$. In the far-field, we apply $\epsilon_{11}^0 = -\epsilon_{22}^0 = 0.02$. The elastic constants are $\mu^M = 1$, $\mu^P = 0.5$ and $\nu^M = \nu^P = 0.2$. The two circular precipitates are initially centered at $(-10, -7.5)$ and $(10, 7.5)$. As we can see in Fig. 3(c), the results from both formulations agree completely.

Putting these quantitative tests and comparisons together, we are convinced the rescaled formulation works as expected. Next we perform long time simulations to study the nonlinear dynamics of multiple precipitates.

5.2 Diffusion with a constant flux $J = \bar{J}$

We perform a long time simulation using three precipitates, two of which have identical shapes with radii given by $r = 2(1 + 0.05(\cos 3\theta + \sin 2\theta))$ and centered at $(-7, -7)$ and $(-14, 14)$. The third precipitate is centered at $(7, 7)$ and has radius $r = 1 + 0.05(\cos 3\theta + \sin 2\theta)$. The far-field flux is $J = 10$. We begin the computation using $N = 1024$ marker points on each interface and the number increases to $N = 16,384$ by the end of the simulation. We double the number of points on each interface when the shape needs refinement.

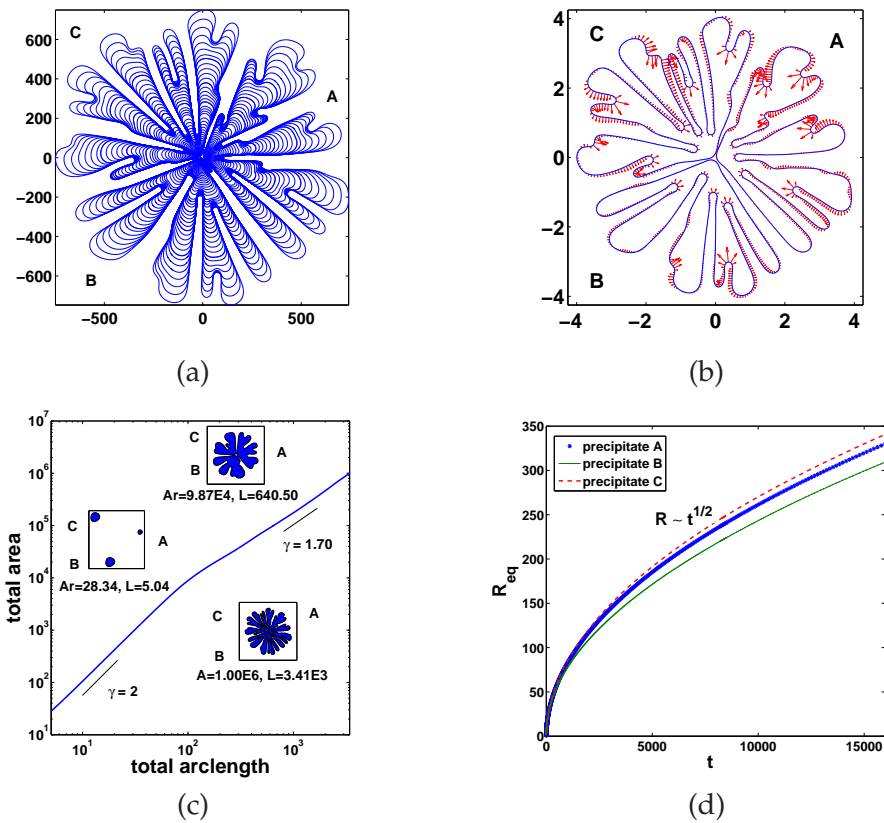


Figure 4: (a) Evolution of three particles in the absence of elastic stresses ($Z=0$). Two of the particles have initial radii $2(1+0.05(\cos 3\theta + \sin 2\theta))$ and are initially located at $(-7, -7)$ and $(-14, 14)$. The third precipitate has initial radius $r = 1 + 0.05(\cos 3\theta + \sin 2\theta)$ and is initially positioned at $(7, 7)$. The flux is $J = 10$. (b) The normal velocity of the marker points on the scaled interface is shown at $\bar{t} = 4.715$. (c) The evolution of the total area as a function of the total arclength in the original frame for the precipitates shown in Fig. 4(a). (d) The evolution of the equivalent radii R_{eq}^i of each precipitate as a function of time in the original frame.

That is, if we observe the area calculation in the rescaled frame is less than five significant digits after the decimal point compared with the exact value \bar{A} ($t=0$), we perform the doubling of the points on the interface. During the doubling, we apply interpolation in the Fourier space to compute the unknown interpolated values with spectral accuracy. In addition, we begin the computation in serial mode. At the later stages of the computation, however, we use up to 4 processors. The marker points are distributed to different processors and each processor is responsible for computing the contributions of the marker points under its control. Also the marker points are distributed in such a way that work load of each processor is evenly distributed [10]. The time step for this computation is 5×10^{-5} . The evolution of these precipitates is shown in Fig. 4. All the particles evolve into ramified fingering patterns, with the overall pattern being reminiscent of the result from the evolution of a single particle [14, 15].

Interestingly, at late stages of the evolution the particles do not merge. Instead, narrow channels form between the precipitates. The normal velocity of the interfaces, which is shown in Fig. 4(b) at $\bar{t}=4.715$, indicates that the velocity of the channels is much smaller than that elsewhere on the precipitate.

In Fig. 4(c), we plot the total area in the original frame, $A = R^2 \bar{A}$, as a function of the total arclength in the original frame $L = R \bar{L} = R \sum_i \bar{L}^i$. We generally find that $A \sim L^\gamma$ where $\gamma = 2$ at early times and decreases below 2 at late times $A \sim L^{1.7}$. In Fig. 4(d), we plot the evolution of equivalent radii $R_{eq}^i = \sqrt{A^i/\pi}$ versus time for the three particles. It is evident that the precipitates are growing at different rates and the one originally at $(-14,14)$ grows faster than other two. This is because this precipitate is farther from the origin and is closer to the flux of matter from the far-field and thereby receives more mass than the other precipitates. The overall growth rate is $R_{eq} \sim t^{1/2}$ as expected for a constant flux.

5.3 Diffusion with flux $J = \bar{J}/R$, $\bar{J} = \text{constant}$

In the context of a single precipitate, Li et al. [26] demonstrated that the Mullins-Sekerka instability can be suppressed if a time-dependent flux $J = \bar{J}/R(t)$, where \bar{J} is a constant, is used. In fact, for a single particle, Li et al. showed that the evolution tends to an attractive self-similarly evolving shape that depends on \bar{J} .

Here, we consider the growth of several precipitates under this time-dependent flux condition. As a test case, we use the same initial precipitate configuration as in Fig. 4. The results are shown in Fig. 5. The most significant feature is that there is no tip splitting and the particles grow with compact morphologies. The possibility of self-similar growth is currently being investigated. In Figs. 5(b) and 5(c) the total area and equivalent radii for the three precipitates are shown for this simulation. We observe that $A \sim L^2$, reflecting the stable growth and that the particle at $(-14,14)$ grows fastest, for the same reason as

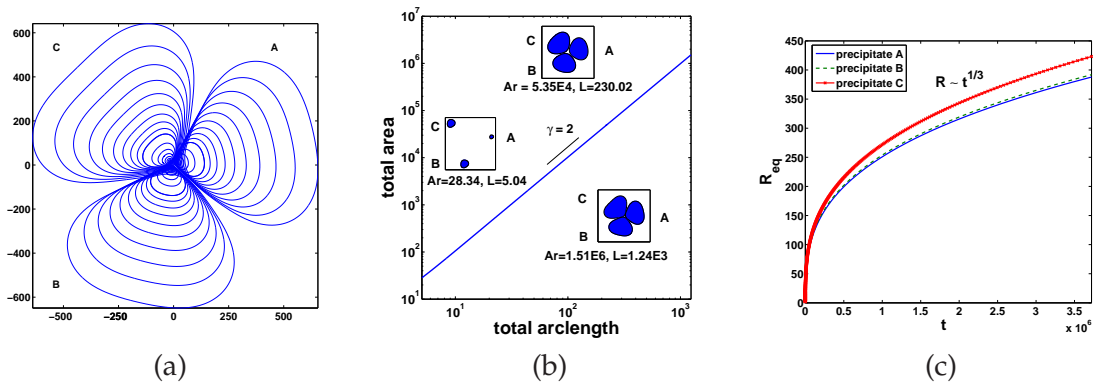


Figure 5: (a) The evolution of precipitates with initial positions and shapes as in Fig. 4, but with flux $J=10/R$. (b) The evolution of the total area versus the total arclength in the original frame for the precipitates shown in Fig. 5(a). (c) The evolution of the precipitate equivalent radii R_{eq}^i versus time in the original frame.

stated earlier. The other two particles grow almost at the same rate. All equivalent radii grow at a slower rate, $R_{eq} \sim t^{1/3}$, than in the case when a constant flux is used.

5.4 Elasticity with flux $J = const$

When the precipitates and matrix are elastically stressed, the precipitates tend to align themselves along the principal axes of the applied stress field. In Fig. 6(a), we present a simulation of three precipitates initially centered at $(15,0)$, $(0,15)$ and $(0,-15)$ and having unit radii initially, under a flux $J=15$. We set $Z=6000$ and the far-field stress $\epsilon_{11}^0 = -\epsilon_{22}^0 = 0.005$. The elastic constants are $\mu^M = 1$, $\mu^P = 0.5$ and $\nu^M = \nu^P = 0.2$.

As the precipitates grow, they acquire dendrite-like shapes with primary arms aligned along the principal axes of the stress field. In this case, the applied shear field effects are comparable to a 4-fold anisotropic surface tension. Fig. 6(b) shows the total area versus

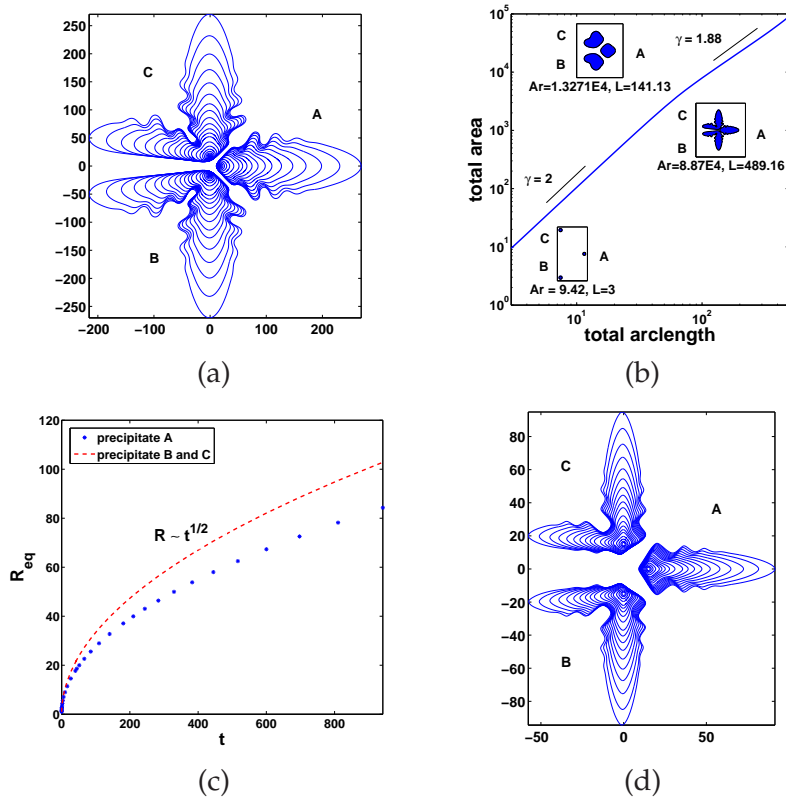


Figure 6: (a) The evolution of three particles initially located at $(15,0)$, $(0,15)$ and $(0,-15)$, with unit radii. The flux is $J=15$, $Z=6000$ and $\epsilon_{11}^0 = -\epsilon_{22}^0 = 0.005$. (b) The total area as a function of total arclength in the original frame. (c) The evolution of the precipitate equivalent radii R_{eq}^i versus time in the original frame for the particles shown in Fig. 6(a). (d) The evolution of the same system of precipitates but with a larger applied strain $\epsilon_{11}^0 = -\epsilon_{22}^0 = 0.02$.

total arclength (in the original frame). Features similar to the diffusion case are observed. At early times, $A \sim L^2$, while at later times $A \sim L^{1.88}$. In Fig. 6(c) we plot the equivalent radii R_{eq}^i versus time in the original frame. Since precipitates B and C evolve identically, we plot the equivalent radius of B only. We that observe precipitates B and C grow faster than precipitate A since they are farther from the origin and receive more mass flux. As in the diffusion case without stress, we observe that $R_{eq}^i \sim t^{1/2}$. In Fig. 6(d), we increase the applied elastic field to $\epsilon_{11}^0 = \epsilon_{22}^0 = -0.02$. This results in a larger tip velocity and side branches that are not as pronounced as in Fig. 6(a).

5.5 Elasticity with flux $J = \bar{J}/R, \bar{J} = constant$

Our previous work in [3] shows that if $J = \bar{J}/R$ and $Z = \bar{Z}/R$ (e.g., applied field is reduced in magnitude like $1/R$) then the Mullins-Sekerka instability can be suppressed and a single precipitate tends to an attractive self-similar shape as it evolves. Here, we test this idea to the case of multiple precipitates. In Fig. 7(a), we present the evolution of three precipitates initially configured as in Fig. 6. The flux $J = 15/R$ and $Z = 6000/R$. The applied field is $\epsilon_{11}^0 = -\epsilon_{22}^0 = 0.005$ and the elastic constants are $\mu^M = 1, \mu^P = 0.5$ and $\nu^M = \nu^P = 0.2$. We observe that the particles grow with compact shapes compared with the dendritic shapes observed in Figs. 6(a) and (d). Further, precipitate A tends to move away from the other two precipitates at late times. In Figs. 7(b) and (c) the total area and equivalent radii of the particles are shown in the original frame. The behavior is similar to that obtained without stress (e.g., Figs. 5(b) and (c)). As in the case without stress, we are investigating further into the possibility of self-similar evolution in this regime.

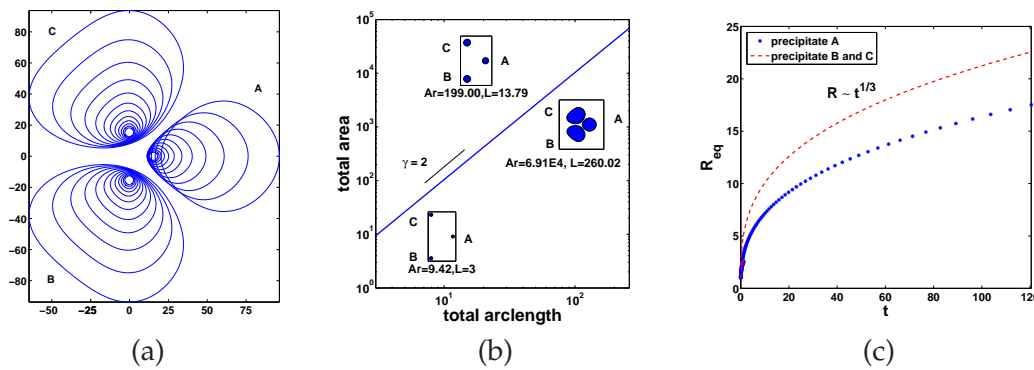


Figure 7: (a) The evolution of three particles with initial locations as in Fig. 6(a), but with flux $J=15/R$ and $Z=6000/R$. (b) The total precipitate area versus the total interface length in the original frame. (c) The evolution of the equivalent radii R_{eq}^i versus time for the case shown in Fig. 7(a).

5.6 Growth and shrinkage at same time with $J > 0$

Up to now, all the precipitates are seen to grow when the applied far-field flux $J > 0$. Here, we present some results to show that shrinkage can also occur even when $J > 0$. In

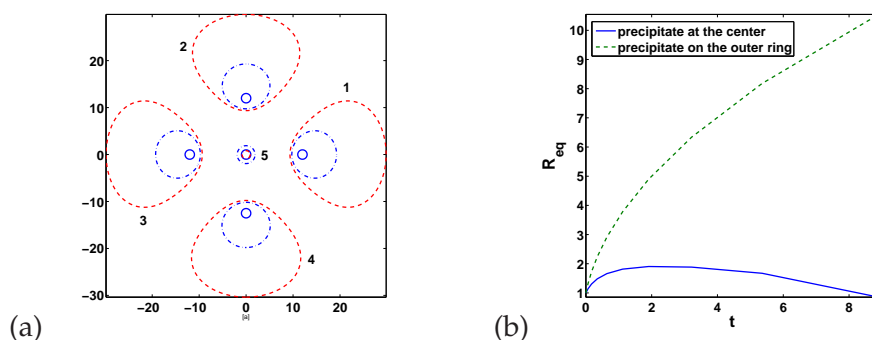


Figure 8: (a) The diffusional evolution of five unstressed ($Z=0$), initially unit circular precipitates. Four precipitates are located on outer ring at a distance of 12.00 units from the origin and the fifth precipitate is placed at the origin. (b) Evolution of R_{eq}^i for the particle at center and particles on the outer circle.

Fig. 8(a) we show the evolution of five unstressed precipitates ($Z=0$) with $J=25$. Four precipitates are placed on the x or y -axes at a distance of 12 units from the origin. The fifth particle is located at the origin (0,0). The solid contours correspond to the initial configuration, the dash-dot contours correspond to an intermediate configuration and the dashed contours correspond to the final configuration of the precipitates. The equivalent radii of the particles R_{eq}^i are plotted in Fig. 8(b). As can be seen from these figures, the four outer precipitates always grow. However, the fifth precipitate grows at early times, but at late times becomes screened from the far-field flux by the four outer precipitates and starts to shrink. This precipitate will vanish after a finite time, as it becomes fully screened from the far-field flux and is subject to a local coarsening process where the system lowers the interfacial energy by diffusing the mass of the fifth precipitate to the other precipitates.

6 Conclusions and future work

We have presented a space-time rescaling scheme to simulate the diffusional evolution of multiple, elastically-stressed precipitates. The scheme allows us to compute complicated morphologies of growing precipitates in a fraction of the cost required used by fixed-frame algorithms. We have shown that when the precipitates are unstressed, the particles tend to acquire a highly ramified structure with the overall shape reminiscent of that of a single particle. In particular, long channels form between the precipitates and precipitate merger is not observed. In presence of applied elastic field, the precipitates form dendrite-like structures with the primary arms aligned in the principal directions of the elastic field. We found that when the far-field flux decreases with the effective radius of the system, tip-splitting and dendrite formation can be suppressed, as in the one particle case. Depending on the initial position of the precipitates, we also observed that some precipitates may shrink while others grow, even when a positive far field flux is applied.

In future work, we will explore the possibility that like single precipitates, multiple precipitates may tend to attractive self-similar configurations under appropriate growth conditions (e.g., $J = \bar{J}/R$ and $Z = \bar{Z}/R$). In addition, the evolution of precipitates under anisotropic surface tension and elastic stresses is another interesting extension of the present work.

Acknowledgments

The authors thank Dr. H.-J. Jou from QuesTek Innovations LLC., Prof. Perry Leo from University of Minnesota and Prof. Qing Nie from University of California-Irvine for stimulating discussions. S. Li also thanks Prof. Yubao Zhen from Harbin Institute of Technology for technical discussions. S. Li acknowledges support from NSF grant DMS-0914923. Some computations in this work were performed on computers acquired using NSF grant (SCREMS) DMS-0923111. J. Lowengrub also thanks the NSF (Division of Mathematical Sciences) for partial support.

References

- [1] N. Akaiwa, K. Thornton and P. W. Voorhees, Large-scale simulations of microstructural evolution of elastically stressed solids, *J. Comput. Phys.*, 173 (2004), 61.
- [2] A. J. Ardell and R. B. Nicholson, On modulated structure of aged ni-al alloys, *Acta Metall.*, 14 (1966), 1225.
- [3] A. Barua, S. Li, X. Li and J. Lowengrub, Self similar evolution of a precipitate in inhomogeneous elastic media, *J. Cryst. Growth*, 351 (2012), 62.
- [4] P. W. Bates, X. Chen and X. Deng, A numerical scheme for the two phase mullins-sekerka problem, *Electron. J. Differential Equations*, 11 (1995), 27.
- [5] T. Belytschko, R. Gracie and G. Ventura, A review of extended/generalized finite element methods for material modeling, *Modell. Simul. Mater. Sci. Eng.*, 17(4) (2009).
- [6] J. Boisse, N. Lecoq, R. Patte and H. Zapolsky, Phase-field simulation of coarsening of gamma precipitates in an ordered gamma matrix, *Acta Mater.*, 55(18) (2007), 6151–6158.
- [7] C. Brebbia, J. Telles and L. Wrobel, *Boundary Element Techniques*, Springer-Verlag, Berlin, 1984.
- [8] H. Cheng, L. Greengard and V. Rokhlin, A fast adaptive multipole algorithm in three dimensions, *J. Comput. Phys.*, 155(2) (1999), 468–498.
- [9] V. Cristini and J. S. Lowengrub, Three-dimensional crystal growth: nonlinear simulation and control of the mullins sekerka instability, *J. Cryst. Growth*, 266 (2004), 552.
- [10] H. Feng, A. Barua, S. Li and X. Li, A fast tree code algorithm for elastic kernel functions, in review, 2012.
- [11] A. Greenbaum, L. Greengard and G. B. McFadden, Laplace equation and dirichlet-neuman map in multiply connected domains, *J. Comput. Phys.*, 105 (1993), 267.
- [12] L. Greengard and J. Helsing, On the numerical evaluation of elastostatic fields in locally isotropic two-dimensional composites, *J. Mech. Phys. Solids*, 46(8) (1998), 1441–1462.
- [13] L. Greengard and V. Rokhlin, A Fast algorithm for particle simulations, *J. Comput. Phys.*, 73(2) (1987), 325–348.

- [14] T. Hou, J. S. Lowengrub and M. Shelley, Removing the stiffness from interfacial flows with surface tension, *J. Comput. Phys.*, 114 (1994), 312.
- [15] H.-J. Jou, P. H. Leo and J. S. Lowengrub, Microstructural evolution in inhomogenous elastic media, *J. Comput. Phys.*, 131 (1997), 109.
- [16] T. Koyama, Simulation of microstructural evolution based on the phase-field method and its applications to material development, *J. Jpn. Inst. Met.*, 73(12) (2009), 891–905.
- [17] Y. Kwon, K. Thornton and P. W. Voorhees, The topology and morphology of bicontinuous interfaces during coarsening, *EPL*, 86(4) (2009).
- [18] Y. Kwon, K. Thornton and P. W. Voorhees, Morphology and topology in coarsening of domains via non-conserved and conserved dynamics, *Philos. Mag.*, 90(1-4) (2010), 317–335.
- [19] I. Lashuk, A. Chandramowlishwaran, H. Langston, T.-A. Nguyen, R. Sampath, A. Shringarpure, R. Vuduc, L. Ying, D. Zorin and G. Biros, A massively parallel adaptive fast multipole method on heterogeneous architectures, *Commun. ACM*, 55(5) (2012), 101–109.
- [20] P. H. Leo and Heng Jeng Jou, Shape evolution of an initially circular precipitate growing by diffusion in an applied stress field, *Acta Metall.*, 41 (1993), 2271.
- [21] P. H. Leo, J. S. Lowengrub and Q. Nie, Microstructural evolution in orthotropic elastic media, *J. Comput. Phys.*, 157 (2000), 44.
- [22] P. H. Leo and R. F. Sekerka, The effect of elastic fields on the morphological stability of a precipitate grown from solid solution, *Acta Metall.*, 37 (1989), 3139.
- [23] B. Li, J. S. Lowengrub, A. Raetz and A. Voigt, Geometric evolution laws for thin crystalline films: modeling and numerics, *Commun. Comput. Phys.*, 6(3) (2009), 433–482.
- [24] S. Li and X. Li, A boundary integral method for computing the dynamics of an epitaxial island, *SIAM J. Sci. Comput.*, 33 (2011), 3282.
- [25] S. Li, J. Lowengrub, J. Fontana and P. Palffy-Muhoray, Control of viscous fingering patterns in a radial hele-shaw cell, *Phys. Rev. Lett.*, 102 (2009), 174501.
- [26] S. Li, J. Lowengrub and P. Leo, A rescaling scheme with application to the long time simulation of viscous fingering in a hele-shaw cell. *J. Comput. Phys.*, 225 (2007), 554.
- [27] X. Li, K. Thornton, Q. Nie, P. W. Voorhees and J. S. Lowengrub, Two- and three-dimensional equilibrium morphology of a misfitting particle and the gibbs-thomson effect, *Acta Mater.*, 52(20) (2004), 5829–5843.
- [28] K. Lindsay and R. Krasny, A particle method and adaptive treecode for vortex sheet motion in three-dimensional flow, *J. Comput. Phys.*, 172(2) (2001), 879–907.
- [29] Y. J. Liu, A fast multipole boundary element method for 2D multi-domain elastostatic problems based on a dual BIE formulation, *Comput. Mech.*, 42(5) (2008), 761–773.
- [30] A. Maheshwari and A. J. Ardell, Morphological evolution of coherent misfitting precipitates in anisotropic elastic media, *Phys. Rev. Lett.*, 70 (1993), 2305.
- [31] S. G. Mikhailin, *Integral Equation and Their Applications to Certain Problems of Mechanics*, Pergamon, New York, 1957.
- [32] W. Mullins and R. F. Sekerka, Morphological stability of a particle growing by diffusion of heat flow, *J. Appl. Phys.*, 34 (1963), 323.
- [33] D. Perez and L. J. Lewis, Multiscale model for microstructure evolution in multiphase materials: application to the growth of isolated inclusions in presence of elasticity, *Phys. Rev. E*, 74(3) (2006).
- [34] R. S. Qin and H. K. Bhadeshia, Phase field method, *Mat. Sci. Technol.*, 26(7) (2010), 803–811.
- [35] R. S. Sampath and G. Biros, A parallel geometric multigrid method for finite elements on octree meshes, *SIAM J. Sci. Comput.*, 32(3) (2010), 1361–1392.

- [36] J.-S. Sohn, Y.-H. Tseng, S. Li, J. Lowengrub and A. Voigt, Dynamics of multicomponent vesicles in a viscous fluid, *J. Comput. Phys.*, 229 (2010), 119.
- [37] I. Steinbach, Phase-field models in materials science, *Modell. Simul. Mater. Sci. Eng.*, 17(7) (2009).
- [38] C. H. Su and P. W. Voorhees, Dynamics of precipitate evolution in elastically stressed solids. i. inverse coarsening, *Acta Mater.*, 44 (1996), 1987.
- [39] C. H. Su and P. W. Voorhees, Dynamics of precipitate evolution in elastically stressed solids. ii. particle alignment, *Acta Mater.*, 44 (1996), 2001.
- [40] M. E. Thompson, C. S. Su and P. W. Voorhees, Equilibrium shape of a misfitting precipitate, *Acta Metall.*, 42 (1994), 2107.
- [41] K. Thornton, N. Akaiwa and P. W. Voorhees, Large-scale simulations of ostwald ripening in elastically stressed solids. coarsening kinetics and particle size distribution, *Acta Mater.*, 52 (2004), 1365.
- [42] K. Thornton, N. Akaiwa and P. W. Voorhees, Large-scale simulations of ostwald ripening in elastically stressed solids. development of microstructure, *Acta Mater.*, 52 (2004), 1353.
- [43] K. Thornton, J. Argen and P. W. Voorhees, Modelling the evolution of phase boundaries in solids at the meso- and nano-scales, *Acta Mater.*, 51 (2003), 5675.
- [44] P. W. Voorhees, R. F. Boisvert and W. C. Johnson, On the morphological development of second phase particles in elastically stressed solids, *Acta Metall.*, 40 (1992), 2979.
- [45] P. W. Voorhees, R. F. Boisvert, G. B. McFadden and D. I. Meiron, Numerical simulation of morphological development during ostwald ripening, *Acta Metall.*, 36 (1988), 207.
- [46] R. Wada, N. Kobayashi, T. Fujii, S. Onaka and M. Kato, Effects of elastic interaction energy and interface energy on morphology and distribution of precipitates: two-dimensional analysis based on anisotropic elasticity, *J. Jpn. Inst. Met.*, 71(8) (2007), 587–591.
- [47] Q. X Wang, Variable order revised binary treecode, *J. Comput. Phys.*, 200(1) (2004), 192–210.
- [48] Y. Wang and J. Li, Phase field modeling of defects and deformation, *Acta Mater.*, 58(4) (2010), 1212–1235.
- [49] L. Ying, G. Biros and D. Zorin, A kernel-independent adaptive fast multipole method in two and three dimensions, *J. Comput. Phys.*, 196 (2004), 591.